Supplementary Information

Rendering metals ultralow modulus and nearly hysteresis-free and linear super-elastic

Jiaming Zhu,[a,b] Yipeng Gao,[c] Dong Wang,[a] Ju Li [e], Tong-Yi Zhang,*, [d] and Yunzhi Wang*,[c]

[a] Center of microstructure science, Frontier Institute of Science and Technology, Xi'an Jiaotong University, Xi'an 710049, China.

[b] Department of Mechanical Engineering, Hong Kong University of Science and Technology, Clear Water Bay, Kowloon, Hong Kong, China.

[c] Department of Materials Science and Engineering, The Ohio State University, 2041 College Road, Columbus, OH 43210, USA.

[d] Materials Genome Institute, Shanghai University, 333 Nanchen Road, Shanghai 200444, China.

[e] Department of Nuclear Science and Engineering and Department of Materials Science and Engineering, Massachusetts Institute of Technology, Cambridge, MA 02139, USA.

Development of phase field model

The phase field model is developed based on the combination of Landau theory[1], gradient thermodynamics[2], and Khachaturyan–Shatalov's microelasticity theory[3]. It should be pointed out that the phase field model is tested (with a uniform Nb concentration of 15 at.%) by producing a stress-strain curve that is consistent with the experimental result of Ti2448 that has the same Nb concentration including the critical stress for the MT, stress hysteresis and superelasticity (see Figure S1).

a) Symmetry breaking during MT in TiNb-based SMAs. The phase filed model is formulated for the multifunctional β TiNb-based alloys. According to the Burgers lattice correspondence[4] for the β (BCC, point group $m\bar{3}m$) to α″ martensite (orthorhombic, point group *mmm*) transformation[5]

$$[001]_{\beta}\rightarrow[100]_{\alpha''},\ [1\bar{1}0]_{\beta}\rightarrow[010]_{\alpha''},\ [110]_{\beta}\rightarrow[001]_{\alpha''},$$

and the symmetry operations in the point groups that preserve such a lattice correspondence, only 8 operations (out of the 48 symmetry operations in $m\bar{3}m$)[6] are left after the transformation, leading to 6 (=48/8) crystallographic equivalent deformation modes (or correspondence variants)[7] characterized by 6 different transformation strain tensors. In fact, because internal shuffle of $\{110\}_{\beta}$ atomic planes is also involved during the transformation[8–10], which doubles the deformation variants, there are total 12 deformation variants[11]. However, an internal shuffle dose not contribute to the transformation strain[12]. Thus, if we choose the three orthogonal axes of the cubic crystal of the parent phase as the reference coordinate system and follow the Burgers correspondence, the transformation matrices that map the parent phase lattice onto that of the martensitic variants by a uniform affine deformation read

$$U_1=\begin{bmatrix}\zeta & 0 & 0\\ 0 & \frac{\alpha+\gamma}{4} & \frac{\gamma-\alpha}{4}\\ 0 & \frac{\gamma-\alpha}{4} & \frac{\alpha+\gamma}{4}\end{bmatrix},\quad U_2=\begin{bmatrix}\zeta & 0 & 0\\ 0 & \frac{\alpha+\gamma}{4} & \frac{\alpha-\gamma}{4}\\ 0 & \frac{\alpha-\gamma}{4} & \frac{\alpha+\gamma}{4}\end{bmatrix},$$

$$U_3 = \begin{bmatrix} \frac{\alpha+\gamma}{4} & 0 & \frac{\gamma-\alpha}{4} \\ 0 & \zeta & 0 \\ \frac{\gamma-\alpha}{4} & 0 & \frac{\alpha+\gamma}{4} \end{bmatrix}, \quad U_4 = \begin{bmatrix} \frac{\alpha+\gamma}{4} & 0 & \frac{\alpha-\gamma}{4} \\ 0 & \zeta & 0 \\ \frac{\alpha-\gamma}{4} & 0 & \frac{\alpha+\gamma}{4} \end{bmatrix},$$

$$U_5 = \begin{bmatrix} \frac{\alpha+\gamma}{4} & \frac{\gamma-\alpha}{4} & 0 \\ \frac{\gamma-\alpha}{4} & \frac{\alpha+\gamma}{4} & 0 \\ 0 & 0 & \zeta \end{bmatrix}, \quad U_6 = \begin{bmatrix} \frac{\alpha+\gamma}{4} & \frac{\alpha-\gamma}{4} & 0 \\ \frac{\alpha-\gamma}{4} & \frac{\alpha+\gamma}{4} & 0 \\ 0 & 0 & \zeta \end{bmatrix}. \tag{1}$$

where $\alpha = \sqrt{2}b/a_0$, $\zeta = a/a_0$, $\gamma = \sqrt{2}c/a_0$, with a_0, a, b and c being the lattice parameters of the parent and martensitic phase. The corresponding stress-free transformation strain (SFTS) of the *p*-th variant, $\varepsilon_{ij}^0(p)$, can be calculated directly from the transformation matrices given in Eq. (1) according to the following equation

$$\varepsilon_{ij}^0(p) = \frac{1}{2}\left(U_p^T U_p - I\right), \ (p = 1 \sim 6), \tag{2}$$

where the superscript *T* indicates matrix transpose, and ***I*** is the identity matrix. The Green strain tensor is more appropriate to describe the MT induced finite deformation and thus adopted in this study, as shown in Eq. (2). As this, second Piola-Kirchhoff stress tensor is used here and the constitutive equation is the generalized Hooke's law, as indicated by Eq. (10).

Note that we are considering a compositionally non-uniform system in the current study and the lattice parameters of the parent and martensitic phases are functions of local concentration, which makes the SFTS in Eq. (2) a function of location as well. Both experimental measurements[13] and *ab initio* calculations[14] show that the concentration-dependence of lattice parameters of β and α″ phases in TiNb alloys can be approximated by linear functions (i.e., following the Vegard's law). Therefore the variation of lattice parameters of β and α″ phases with concentration is obtained by fitting the experimental and simulation data reported in references[5,13–16],

$$a_0 = 3.296 + 1.3 \times c_{Nb} \times 10^{-4} \text{ Å}, \tag{3a}$$

$$a = 2.894 + 1.2 \times c_{Nb} \times 10^{-2} \text{ Å}, \tag{3b}$$

$$b = 5.167 - 1.7 \times c_{Nb} \times 10^{-2} \text{ Å}, \tag{3c}$$

$$c = 4.748 - 4.8 \times c_{Nb} \times 10^{-3} \text{ Å}, \tag{3d}$$

where c_{Nb} is the Nb concentration in atomic percent. Besides the SFTS, the M_s also depends on Nb concentration, which, according to existing data in the literature[17–19], can be approximated by the following linear relationship

$$M_s = 550 - 24 \times c_{Nb} \text{ K}. \tag{4}$$

b) Free energy formulation. In our phase field approach, the parent and martensitic phases in TiNb-based alloys are characterized by using six non-conserved structural order parameters, η_p (p=1~6), with $(\eta_{p=1\sim6} = 0)$ representing the parent phase and $(\eta_p = \pm 1,\ \eta_{q=1\sim6,\ but\ q \neq p} = 0)$ representing the p-th correspondence variant of the martensitic phase, where +1 and -1 denote atomic shuffles in two opposite directions in a correspondence variant. The total free energy functional, F, of the system is formulated as the following

$$F = \int \left[\frac{1}{2} \kappa_\eta \sum_{p=1}^{6} (\nabla \eta_p)^2 + f_{ch}(\eta_1, \cdots \eta_6) + f_{ex}(\eta_1, \cdots \eta_6) \right] d^3 r + E_{el}, \tag{5}$$

where κ_η is the gradient energy coefficient for structural non-uniformities following the gradient thermodynamics[2], f_{ch} is the Landau free energy that describes the free energy of a local volume element having a uniform structural state characterized by $\eta_p(\mathbf{r})$ (p=1-6)[20–23]. In the current study, the stress-free transformation strain tensor for a local volume element located at $\boldsymbol{r}$ will be given by

$$\varepsilon_{ij}^{MT}(r) = \sum_{p=1}^{6} \varepsilon_{ij}^{0}(p, r) \eta_p^2(r) \tag{6}$$

and the Landau free energy can be approximated by the following polynomial[24]

$$f_{ch}(\eta_1, \cdots \eta_6) = \frac{1}{2}A_1(T - T_0)\sum_{p=1}^{6}\eta_p^2(r) - \frac{1}{4}A_2\sum_{p=1}^{6}\eta_p^4(r) + \frac{1}{6}A_3\left(\sum_{p=1}^{6}\eta_p^2(r)\right)^3, \quad (7)$$

where A_1, A_2 and A_3 are expansion coefficients. The M_s modulation induced by concentration modulation (CM) is incorporated into the model by formulating T_0 as a function of concentration, i.e., $T_0 = 493 - 24 \times c_{Nb}$ K.

The free energy associated with an external stress, σ_{kl}, (i.e., the work term by the external stress) in Eq. (5), is given by the following equation

$$f_{ex}(\eta_1, \cdots \eta_6) = -\sigma_{kl} \cdot \varepsilon_{kl}^{MT}(r). \quad (8)$$

The last term in Eq. (5), E_{el}, is the coherency elastic strain energy of a structurally non-uniform but coherent system (i.e., martensitic variants coherently embedded in the parent phase matrix) characterized by $\eta_p(\mathbf{r})$. According to the literature[25], in which a new mathematical formulation of the coherency elastic strain energy that accounts for CM is derived based on Khachaturyan–Shatalov's microelasticity theory (KS-theory)[3], it has the following close form

$$E_{el} = \frac{1}{2}\sum_{K=1}^{9}\sum_{L=1}^{9}\int \frac{d^3k}{(2\pi)^3}B_{KL}(n)\{\theta_K\}_k\{\theta_L\}_k^*, \quad (9)$$

where the integral is taken in the reciprocal space, $n = \frac{k}{k}$ is a unit vector and k is a vector with a modulus of k in the reciprocal space (note that $k = 0$ is to be excluded from the integration), $\{\theta_K\}_k$ represents the Fourier transformation of θ_K, which is defined as $\theta_K(r) = \sum_{p=1}^{6}\left[\varepsilon_{ij}^0(p, r) \cdot \eta_p^2(r)\right]$ (the indices i, j and K in this expression are correlated via a generalized Voigt notation, i.e. 11 →1, 22 →2, 33 →3, 23 →4, 13 →5, 12 →6, 32 →7, 31 →8, 21 →9). Note that the transformation strain, $\varepsilon_{ij}^0(p, r)$, is a function of position because of its dependence on local concentration[13,16]. For a system with a free boundary, $B_{KL}(n)$ in Eq. (9) reads

$$B_{KL}(n) = \begin{cases} 0 & n = 0 \\ C_{ijkl}\varepsilon_{ij}^{new}(K)\varepsilon_{kl}^{new}(L) - n_i\sigma_{ij}^{new}(K)\Omega_{jk}(n)\sigma_{kl}^{new}(L)n_l & n \neq 0 \end{cases}, \quad (10)$$

where $\sigma_{ij}^{new}(K) = C_{ijkl}\varepsilon_{kl}^{new}(K)$, $\Omega_{ij}^{-1}(n) = C_{iklj}n_k n_l$, and

$$\varepsilon_{kl}^{new}(K) = \begin{cases} 1 & if\ K\ is\ Voigt\ notation\ of\ kl \\ 0 & otherwise \end{cases}.$$

Note that such a boundary condition is required to simulate stress-controlled (constant stress) uniaxial tension.

c) Kinetic equation. The following time-dependent Ginzburg-Landau equation[26] is used to describe the temporal and spatial evolution of the structural order parameters during the MT

$$\frac{d\eta_p(r,t)}{dt} = -M\frac{\delta F}{\delta \eta_p(r,t)} + \xi_p(r,t),\ p = 1 \sim 6 \quad , \tag{11}$$

where M is the kinetic coefficient and $\xi_p(r,t)$ are the Langevin noise terms for structural fluctuations, which meets the following fluctuation-dissipation theorem[20,24]:

$$\left\langle \xi_p(r,t)\xi_p(r',t') \right\rangle = 2\frac{k_B T}{|\Delta f| l_0^3}\delta(r-r')\delta(t-t') \quad . \tag{12}$$

where k_B is the Boltzmann constant, T is the absolute temperature, $|\Delta f|$ is the chemical driving force (free energy difference between the parent and martensitic phases calculated from the Landau free energy), l_0 is the length scale assigned to the computational grid increment, and δ is the Kronecker delta function.

Equation (11) is solved numerically in the reciprocal space using a finite difference method for a compositionally modulated model system. The total free energy of the parent phase at 773K (a temperature above M_s) is formulated on the basis of the Ti-Nb binary system[2,27–29] in our spinodal decomposition model,

$$F^{SD} = \int_V \left\{ f(c) + \frac{\kappa_c}{2}(\nabla c)^2 \right\} dV \quad , \tag{13}$$

where $f(c)$ is the local chemical free energy, c is Nb concentration, and κ_c is the gradient energy coefficient. The dimensionless local chemical free energy $f^*(c)$ approximated by a double-well function with the equilibrium concentrations of the two coexisting phases being 0.08 and 0.2[18],

respectively, e.g., $f^*(c) = (c - 0.08)^2(0.2 - c)^2$. The dimensionless gradient energy coefficient is chosen to be $\kappa_c^* = 0.691$. The reduced time is calculated via $t^* = \frac{M_c|\Delta f_c|}{l_0^2}t$, where M_c denotes chemical mobility of composition, $|\Delta f_c|$ is chemical driving force of spinodal decomposition, l_0 is numerical grid size. The dimensionless time step Δt^* is chosen to be 0.001. The interfacial energy between the solute-rich and solute lean phases at equilibrium is assumed to be ~0.01 J/m^2, which yields a numerical grid size of l_0~1 nm. The temporal evolution of the concentration field is governed by the Cahn-Hilliard equation[30]. The gradient energy coefficient is, in general, a constant for a given material. To study the role of CM wavelength in the linear super-elastic behavior, different dimensionless gradient energy coefficients ($\kappa_c^* =$ 0.058, 0.288, 0.461, 0.691, and 2.591) are used to generate systems with different CM wavelengths (12 nm, 30 nm, 37 nm, 44 nm, and 110 nm, respectively) in spinodal decomposition. The relationship[30] between gradient energy coefficients and CM wavelength, L, is $L = 2\pi\sqrt{-\frac{2\kappa_c}{f''(c)}}$, where $f''(c)$ represents $\frac{d^2f}{dc^2}$. It should be pointed out that such a range of spinodal wavelength is in consistence with experimental observations[31].

d) Model parameters. The elastic constants of the parent phase, C_{11}=57.2 GPa, C_{12}=36.1 GPa and C_{44}=35.9 GPa are obtained from the literature [5,32]. Homogeneous modulus assumption is adopted in this study, i.e. the α″ martensitic phase is assumed to have the same elastic constants as that of the parent phase because of the lack of consistent experimental data for the elastic constants of α″ martensites[33]. The expansion coefficients in the Landau free energy, A_1=1.3×10^5 J/m^3·K, A_2=11.74×10^7 J/m^3, A_3=17.39×10^7 J/m^3, are chosen in such a way that the phase field model (with an uniform Nb concentration of 15 at.%) produces a stress-strain curve that is consistent with the experimental result of Ti2448 that has the same Nb concentration [32], including the critical stress for the MT, stress hysteresis and super-elasticity (see Figure S1). The gradient energy coefficient for the structural non-uniformity is assumed to be κ_η=1.2×10^{-12} J/m, which yields an interfacial energy between the parent and martensitic phases of Γ_{AM} ≈0.01 J/m^2 (which falls in the range of the experimental values[34]) and a twin boundary energy between different martensitic variants of Γ_{MM}≈0.02 J/m^2 (Γ_{MM}≈2Γ_{AM} according to reference [35]) with a length scale of l_0~1 nm. The structural mobility in Eq. (11) is chosen as M=1×10^{-4}

$m^4J^{-1}s^{-1}$, estimated from $v=M(-\Delta f)$[35,36], where v is the interface velocity between the parent and martensitic phases during the MT (~10^3 m/s) and Δf=-10^7 J/m^3 [37,38] is the typical driving force for the MT. The amplitude of the Langevin noise is $2\frac{k_BT}{|\Delta f|l_0^3}=$ 0.3 in our simulations at 300K. The system size used in the simulations is $128^{l_0}\times128^{l_0}\times128^{l_0}$. Periodical boundary conditions are adopted in all three dimensions.

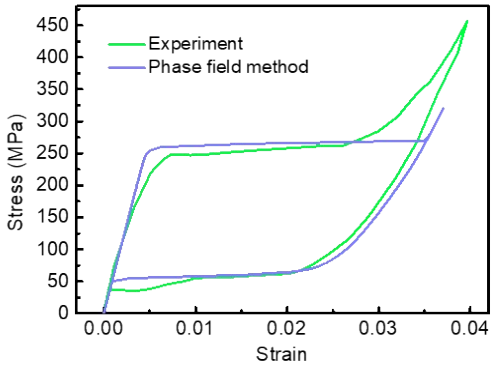

Fig. S1 Comparison between phase field model and experiment. Comparison between stress strain curves obtained respectively from the phase field simulation and experiment[32].

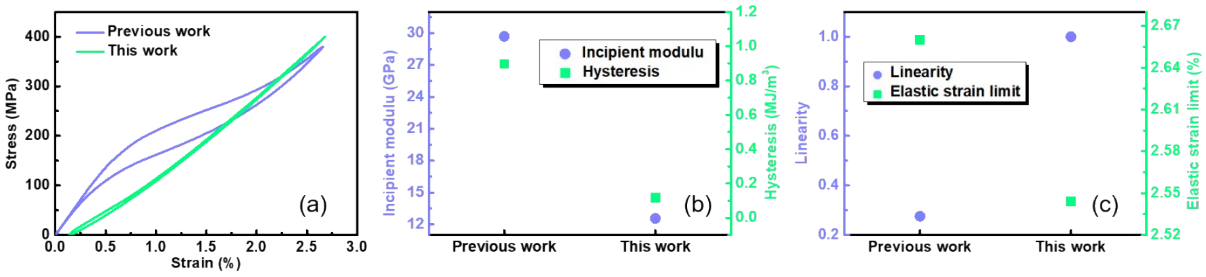

Fig. S2 Comparison of results between previous study (i.e. Reference 44) and this study in (a) stress strain curve, (b) incipient modulus, hysteresis, (c) linearity and elastic strain limit. See Figure 3 for the definition of incipient modulus and linearity.

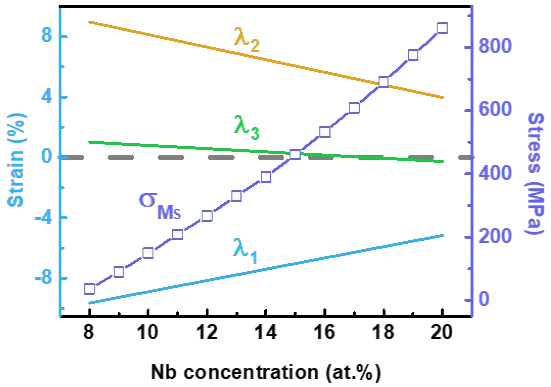

Fig. S3 Dependence of σ_{M_s} and principle strains (λ_1, λ_2 and λ_3) of the stress-free transformation strain of Ti2448 on Nb concentration.

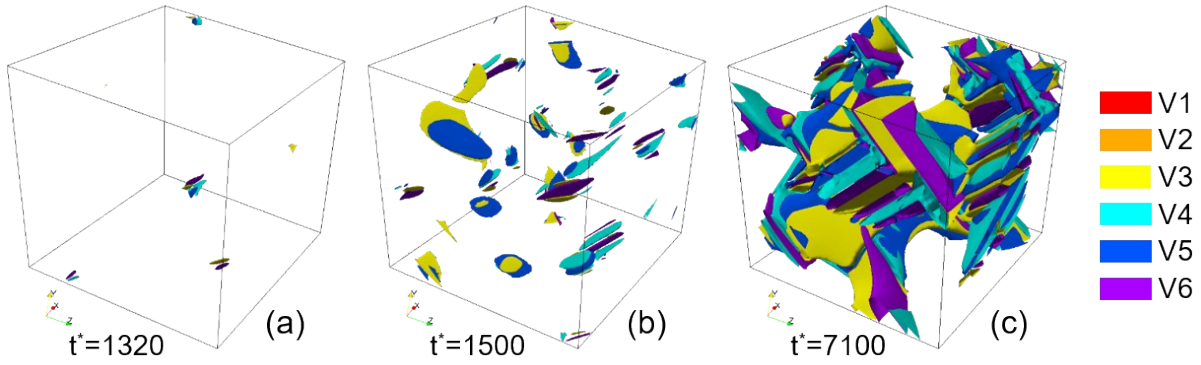

Fig. S4 Residual martensites induced by pre-straining. The residual martensites after the first loading-unloading cycle in CMFMs aged for (a) t^*=1320 (L=38 nm), (b) t^*=1500 (L=42 nm), and (c) t^*=7100 (L=73 nm).

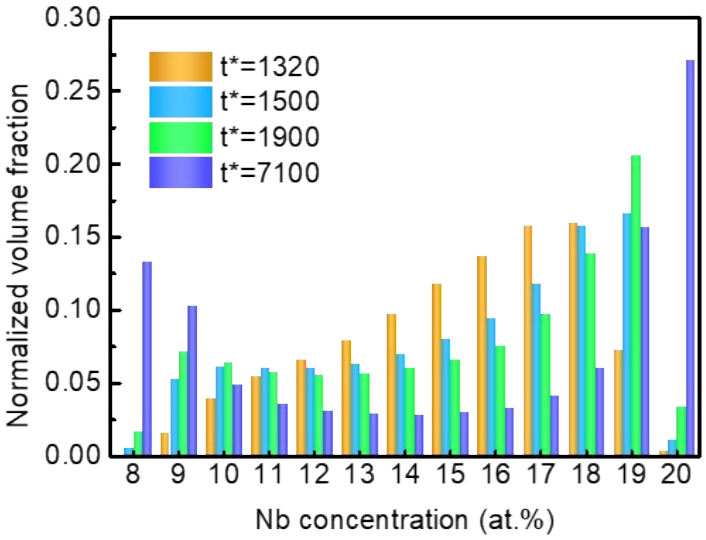

Fig. S5 Statistical distributions of Nb concentration. Statistical distributions of voxels having certain Nb concentration in the computational cell aged for different time.

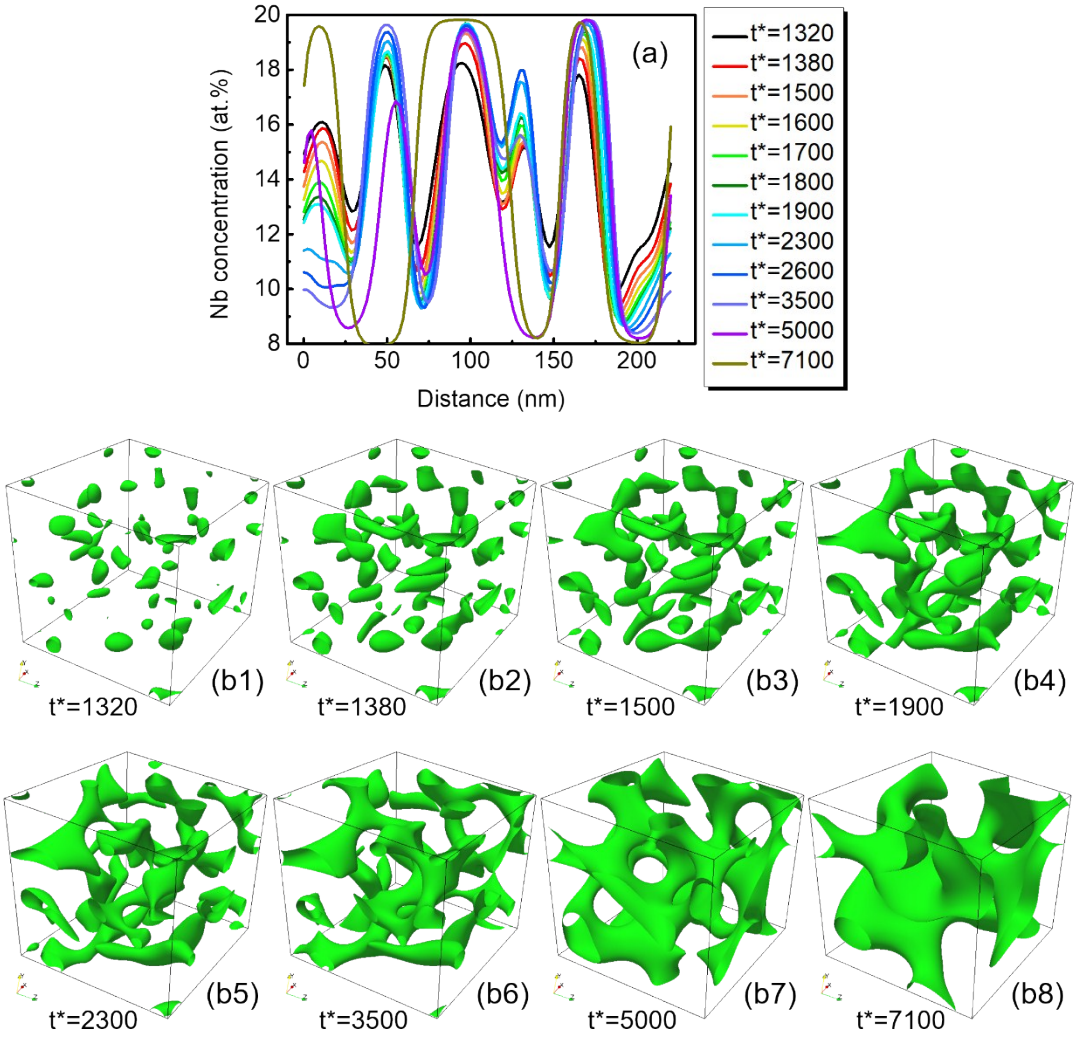

Fig. S6 One dimensional and three dimensional plots of CM at different ageing time during spinodal decomposition. (a) Concentration variation along a body diagonal of simulation systems aged for different time. (b1)-(b8) Evolution of Nb-lean regions that are able to accommodate retained martensites during spinodal decomposition.

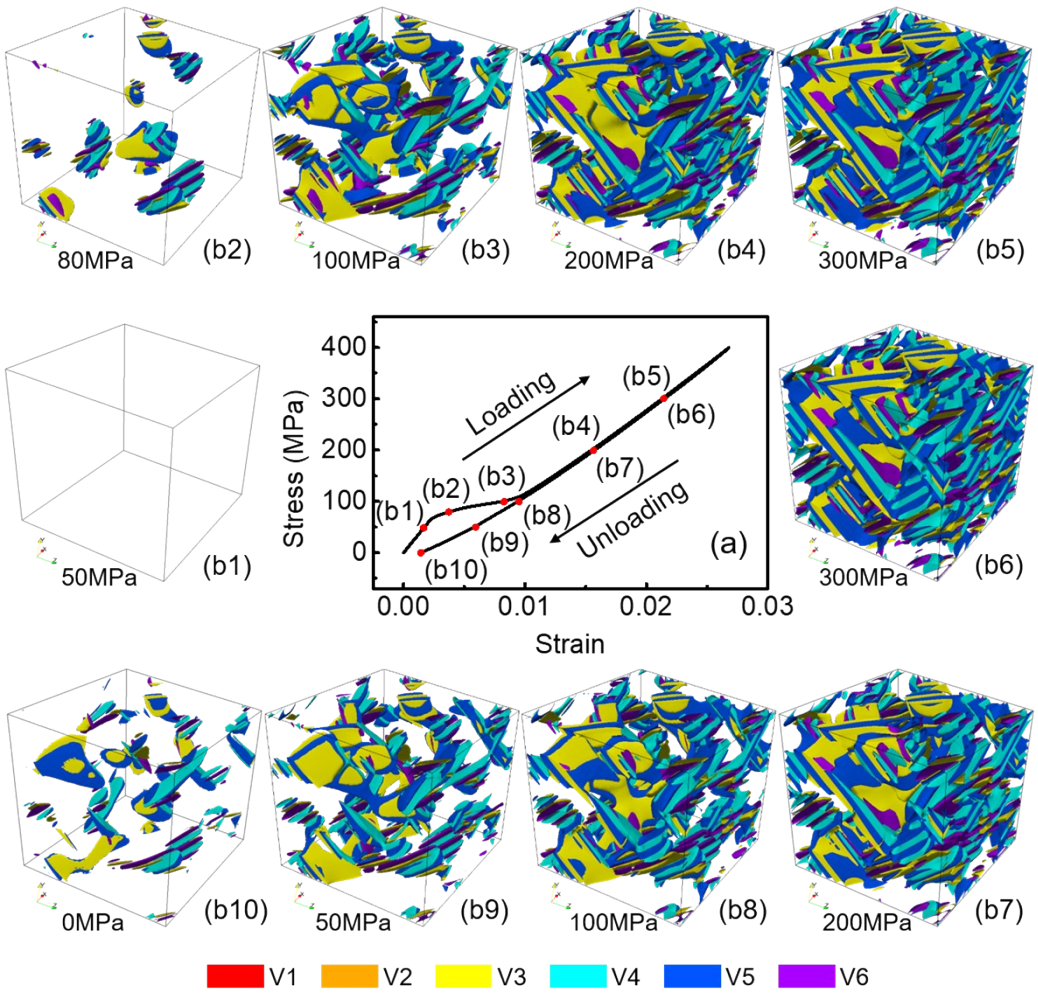

Fig. S7 Stress strain curve and microstructure evolution of the first loading-unloading cycle, i.e. pre-straining process. (b1-b10) show the microstructures at various stress levels marked by (b1-b10) in (a), respectively, during first cyclic loading/unloading. The parent phase is set to be transparent and the martensitic variants (Vs) are plotted as iso-surfaces with different colors, as indicated in the color map at the bottom.

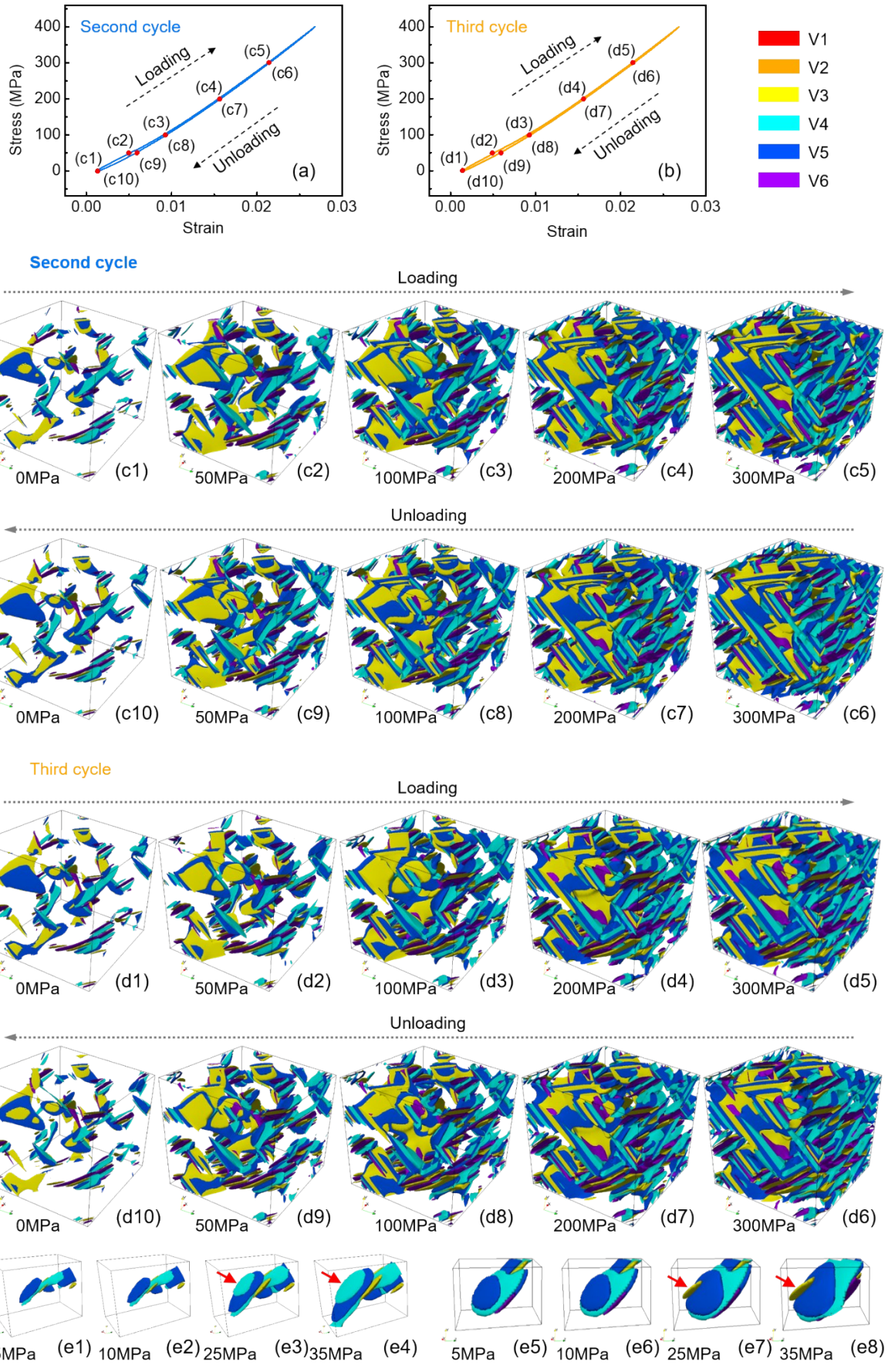
Second cycle
Loading
Unloading
(a)
Stress (MPa)
Strain
Third cycle
(b)
V1
V2
V3
V4
V5
V6
0MPa
50MPa
100MPa
200MPa
300MPa
5MPa
10MPa
25MPa
35MPa

Fig. S8 Microstructural evolution during MT upon the second and third loading-unloading cycles. Stress strain curves of a concentration modulated system having a wavelength of ~44 nm (after ageing at 773 K for t^*=1900) during (a) second and (b) third loading-unloading cycles. (c1-c10) and (d1-d10) show microstructures at various loading-unloading points marked by (c1-c10) in (a) and (d1-d10) in (b), respectively, where the parent phase is set to be transparent and the martensitic correspondence variants (V_i, i=1-6) are plotted as iso-surface contours with different colors, as indicated in the legend at the upper right corner. Red arrows in (e3), (e4), (e7) and (e8) indicate variants generated via local autocatalysis which is defined as the autocatalytic effect happened in a Nb-lean region.

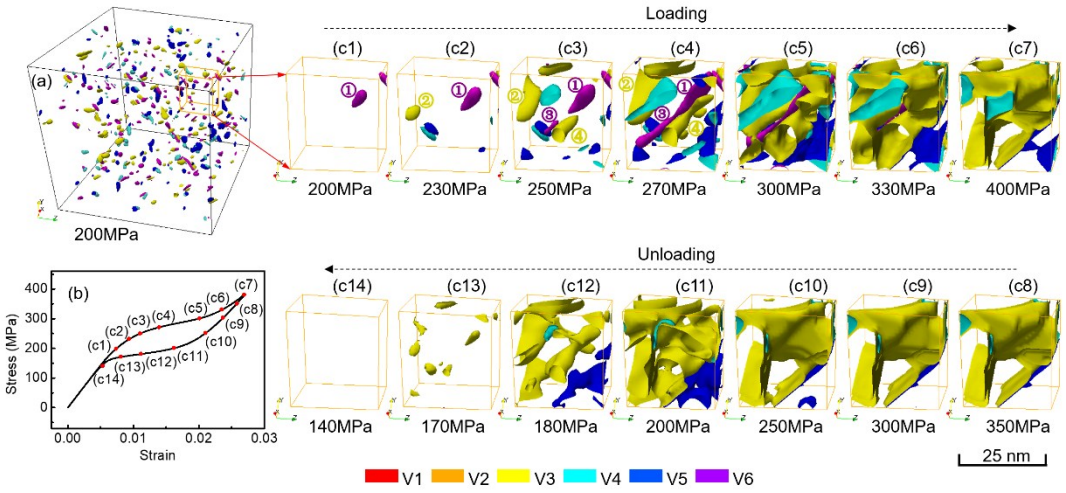

Fig. S9 Martensitic transformation in a system with a concentration wavelength of 12 nm. (a) Microstructure and (b) stress strain curve of a system with a concentration wavelength of 12 nm. (c1)-(c14) are close observations of martensitic particles in a local region during loading and unloading. Circled numbers in (c1)-(c4) indicate single variant martensitic particles of corresponding colors.

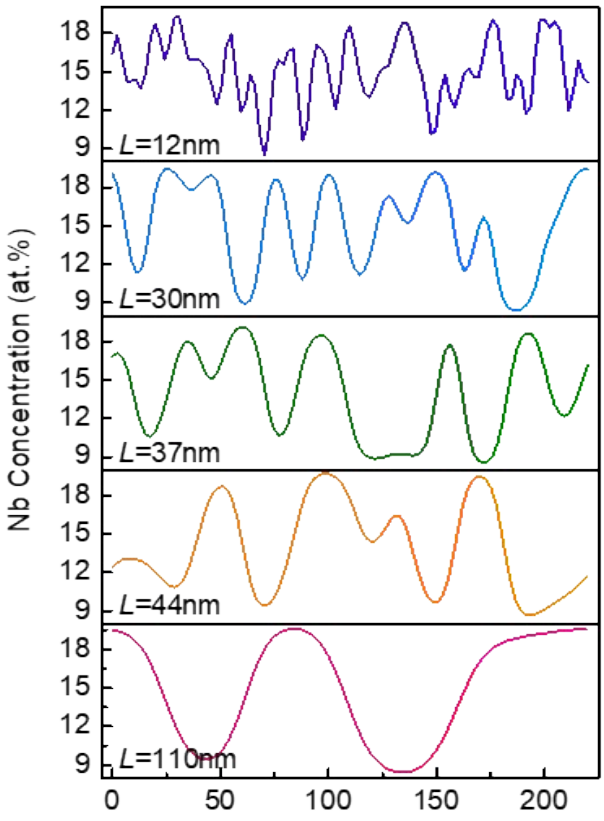

Fig. S10 One dimensional plots of CM. Concentration variation along a body diagonal of simulation systems having different concentration wavelength.

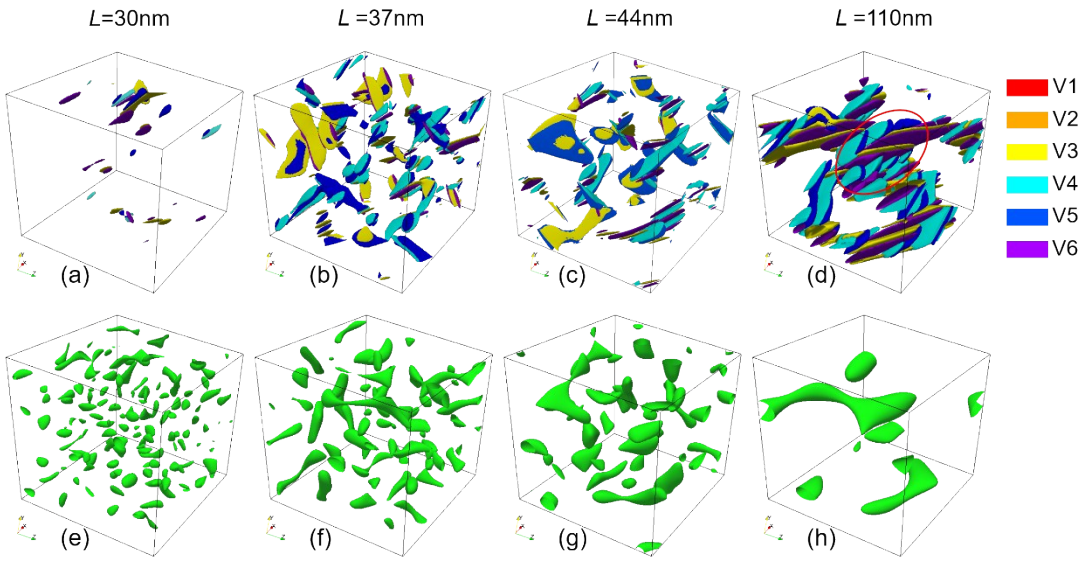

Fig. S11 Retained martensites and Nb-lean regions. (a)-(d) Residual martensites in systems having different concentration wavelength after pre-straining. The red circle indicates a herringbone structure. (e)-(h) Nb-lean regions of corresponding systems are represented by green iso-surface concentration contours. Residual martensites in (a)-(d) are accommodated by Nb-lean regions in (e)-(h).

Geometric Compatibility Analysis

Analysis of average strain of martensitic patterns

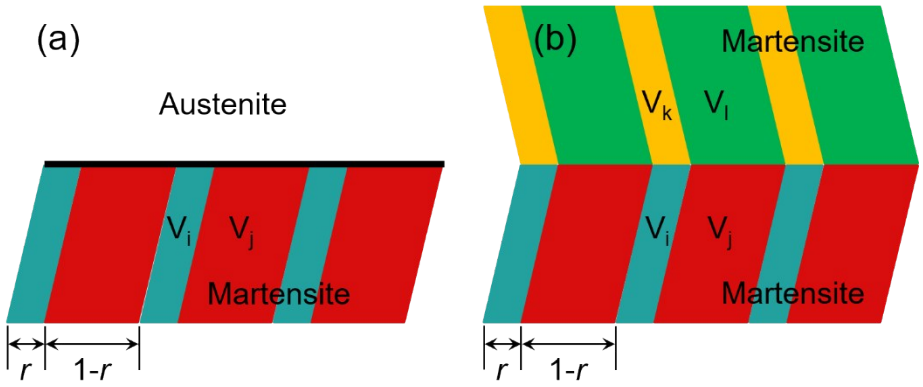

Fig. S12 Schematic drawing of self-accommodating martensitic patterns. (a) 2-variant and (b) 4-variant domain patterns. *r* denotes the volume fraction of a variant in a domain pattern.

The average strain of a 2-variant domain is

$$r\varepsilon^0(i) + (1-r)\varepsilon^0(j). \tag{14}$$

Taking the type-I or type-II twin formed by variant 3 and variant 5 as an example

$$r\varepsilon^0(3) + (1-r)\varepsilon^0(5) =$$

$$\frac{1}{2}\begin{bmatrix} \frac{\alpha^2+\gamma^2}{8} - 1 & (1-r)\frac{\gamma^2-\alpha^2}{8} & r\frac{\gamma^2-\alpha^2}{8} \\ (1-r)\frac{\gamma^2-\alpha^2}{8} & (1-r)\left(\frac{\alpha^2+\gamma^2}{8} - 1\right) + r(\zeta^2-1) & 0 \\ r\frac{\gamma^2-\alpha^2}{8} & 0 & r\left(\frac{\alpha^2+\gamma^2}{8} - 1\right) + (1-r)(\zeta^2-1) \end{bmatrix} \tag{15}$$

The average strain of a 4-variant domain is

$$\frac{1}{2}[r\varepsilon^0(i) + (1-r)\varepsilon^0(j) + r\varepsilon^0(k) + (1-r)\varepsilon^0(l)]. \tag{16}$$

Taking the herringbone structure formed by variant 3, 4, 5 and 6 as an example

$$\frac{1}{2}[r\varepsilon^0(3) + (1-r)\varepsilon^0(5) + r\varepsilon^0(4) + (1-r)\varepsilon^0(6)] =$$

$$\frac{1}{2}\begin{bmatrix} \frac{\alpha^2+\gamma^2}{8}-1 & 0 & 0 \\ 0 & (1-r)\left(\frac{\alpha^2+\gamma^2}{8}-1\right)+r(\zeta^2-1) & 0 \\ 0 & 0 & r\left(\frac{\alpha^2+\gamma^2}{8}-1\right)+(1-r)(\zeta^2-1) \end{bmatrix} \quad (17)$$

Equation (15) demonstrates that, besides the dilation deformation, 2-variant martensitic particles will induce shear deformation in matrix as well. However, 4-variant martensitic particles only cause dilation deformation. Therefore, 2-variant retained martensitic particles should be accompanied by higher elastic energy than 4-variant retained martensitic particles.

Supplementary References

1 L. D. Landau and E. M. Lifshitz, *Statistical physics*, Pergamon Press, Oxford, 1980.

2 J. W. Cahn and J. E. Hilliard, *J. Chem. Phys.*, 1958, **28**, 258.

3 A. G. Khachaturyan, *Theory of Structural Transformations in Solids*, John Wiley & Sons, New York, 1983.

4 W. G. Burgers, *Physica*, 1934, **1**, 561–586.

5 J. Liu, Y. Y. Wang, Y.-L. Hao, Y. Y. Wang, Z. Nie, D. Wang, Y. Ren, Z. Lu, J. Wang, H. Wang, X. Hui, N. Lu, M. J. Kim and R. Yang, *Sci. Rep.*, 2013, **3**, 2156.

6 T. Hahn, *Int. Tables Crystallogr. Vol. A Space-gr. symmetry*, 2006, **2**, 7–11.

7 Y. Gao, R. Shi, J.-F. F. Nie, S. A. Dregia and Y. Wang, *Acta Mater.*, 2016, **109**, 353–363.

8 T. Ahmed and H. J. Rack, *J. Mater. Sci.*, 1996, **31**, 4267–4276.

9 Y. Zheng, R. E. A. Williams, S. Nag, R. Banerjee, H. L. Fraser and D. Banerjee, *Scr. Mater.*, 2016, **116**, 49–52.

10 E. G. Obbard, Y. L. Hao, T. Akahori, R. J. Talling, M. Niinomi, D. Dye and R. Yang, *Acta Mater.*, 2010, **58**, 3557–3567.

11 Y. Gao, N. Zhou, D. Wang and Y. Wang, *Acta Mater.*, 2014, **68**, 93–105.

12 J. W. Christian, *The Theory of Transformations in Metals and Alloys*, Pergamon Press, Oxford, UK, Third., 2002.

13 H. Y. Kim, Y. Ikehara, J. I. Kim, H. Hosoda and S. Miyazaki, *Acta Mater.*, 2006, **54**, 2419–2429.

14 A. Pathak, S. Banumathy, R. Sankarasubramanian and a. K. Singh, *Comput. Mater. Sci.*, 2014, **83**, 222–228.

15 S. Banumathy, R. K. Mandal and a. K. Singh, *J. Appl. Phys.*, 2009, **106**, 093518.

16 T. Inamura, J. I. Kim, H. Y. Kim, H. Hosoda, K. Wakashima and S. Miyazaki, *Philos. Mag.*, 2007, **87**, 3325–3350.

17 Y. L. Hao, S. J. Li, S. Y. Sun and R. Yang, *Mater. Sci. Eng. A*, 2006, **441**, 112–118.

18 Y. L. Hao, H. L. Wang, T. Li, J. M. Cairney, A. V. Ceguerra, Y. D. Wang, Y. Wang, D. Wang, E. G. Obbard, S. J. Li and R. Yang, *J. Mater. Sci. Technol.*, 2016, **32**, 705–709.

19 E. W. Collings, *A Sourcebook of Titanium Alloy Superconductivity*, Springer US, Boston, MA, 1983.

20 E. M. Lifshitz and L. P. Pitaevskii, in *Course of Theoretical Physics*, eds. L. D. Landau and E. M. Lifshitz, Pergamon Press, Oxford, 3rd edn., 1980, vol. 5.

21 Y. A. Izyumov and V. N. Syromyatnikov, *Phase Transitions and Crystal Symmetry*, Kluwer Academic Publishers, Boston, 1990.

22 P. Tolédano and V. Dmitriev, *Reconstructive Phase Transitions*, World Scientific, New Jersey, 1996.

23 Y. Wang and A. G. Khachaturyan, *Mater. Sci. Eng. A*, 2006, **438**–**440**, 55–63.

24 Y. Wang and A. G. Khachaturyan, *Acta Mater.*, 1997, **45**, 759–773.

25 J. Zhu, Y. Gao, D. Wang, T.-Y. Zhang and Y. Wang, *Acta Mater.*, 2017, **130**, 196–207.

26 J. D. Gunton, M. S. Miguel and P. S. Sahni, in *Phase Transitions and Critical Phenomena*, eds. E. C. Domb and J. Lebowitz, Academic Press, London, 1983, vol. 8, pp. 269–466.

27 Y. Lu, C. Wang, Y. Gao, R. Shi, X. Liu and Y. Wang, *Phys. Rev. Lett.*, 2012, **109**, 086101.

28 L.-Q. Chen, *Annu. Rev. Mater. Res.*, 2002, **32**, 113–140.

29 J. Langer, M. Bar-on and H. Miller, *Phys. Rev. A*, 1975, **11**, 1417–1429.

30 J. Cahn, *Acta Metall.*, 1961, **9**, 795–801.

31 F. Findik, *Mater. Des.*, 2012, **42**, 131–146.

32 Y. W. Zhang, S. J. Li, E. G. Obbard, H. Wang, S. C. Wang, Y. L. Hao and R. Yang, *Acta Mater.*, 2011, **59**, 3081–3090.

33 J. Zhu, H. Wu, D. Wang, Y. Gao, H. Wang, Y. Hao, R. Yang, T.-Y. Zhang and Y. Wang, *Int. J. Plast.*, 2017, **89**, 110–129.

34 G. B. Olson and M. Cohen, *Metall. Trans. A*, 1976, **7**, 1897–1904.

35 D. Wang, S. Hou, Y. Wang, X. Ding, S. Ren, X. Ren and Y. Wang, *Acta Mater.*, 2014, **66**, 349–359.

36 C. Huang, D. Browne and S. McFadden, *Acta Mater.*, 2006, **54**, 11–21.

37 J. Khalil-Allafi, W. W. Schmahl and T. Reinecke, *Smart Mater. Struct.*, 2005, **14**, S192.

38 G. Olson and M. Cohen, *Metall. Trans. A*.